

Accurate, precise pressure sensing with tethered optomechanics

O. R. Green,^{*} Y. Bao, J. R. Lawall, J. J. Gorman, and D. S. Barker[†]

National Institute of Standards and Technology, Gaithersburg, MD 20899

(Dated: September 4, 2024)

We show that optomechanical systems can be primary pressure sensors with uncertainty as low as 1.1 % of reading via comparison with a pressure transfer standard. Our silicon nitride and silicon carbide sensors are short-term and long-term stable, displaying Allan deviations compatible with better than 1 % precision and baseline drift significantly lower than the transfer standard. We also investigate the performance of optomechanical devices as calibrated gauges, finding that they can achieve total uncertainty less than 1 %. The calibration procedure also yields the thin-film density of our sensors with state-of-the-art precision, aiding development of other calibration-free optomechanical sensors. Our results demonstrate that optomechanical pressure sensors can achieve accuracy, precision, and drift sufficient to replace high performance legacy gauges.

I. INTRODUCTION

Optomechanical and nanophotonic devices are of great interest due to their potential as small, robust, portable sensors for a variety of physical quantities. Applications of nanophotonic and optomechanical sensors include accelerometry [1], thermometry [2, 3], hygrometry [4], and magnetometry [5]. Optical sensors are advantageous because they leverage tools from optical frequency metrology and spectroscopy to achieve high measurement precision [6, 7]. The small size of nanophotonic and optomechanical devices means that many sensors for disparate physical quantities can be integrated into a single package [8]. Optomechanical systems can self-calibrate using intrinsic quantum [2] or classical noise processes [1], creating a path to compact suites of primary (*i.e.*, calibration-free) sensors. Achieving such sensor suites requires not only a wide array of measurable physical quantities, but also that the constituent sensors have accuracy competitive with legacy technologies.

Sensors based on mechanical damping and deflection have a long history in precision pressure and vacuum metrology [9, 10]. Recently, the principles of such mechanical sensors have been applied in optomechanical systems. The size and sensitivity of optomechanics allows new measurement paradigms, such as extreme squeezed-film enhancement [11] or direct detection of individual gas molecule collisions [12, 13]. When the mass and area of the device are known, optomechanical devices offer calibration-free pressure measurements [14], which have been demonstrated with levitated [15] and tethered [16] devices at approximately 10 % of reading accuracy. However, the demonstrated accuracy and precision of optomechanical pressure sensors are insufficient to replace high performance gauges (with typical accuracy of 1 % or better) in industrial and metrological applications.

Here, we investigate the limits to the accuracy, precision, and long-term stability of tethered silicon ni-

tride and silicon carbide optomechanical pressure sensors. Our sensors convert their gas-collision-induced mechanical damping response into a pressure via prior characterization of their density and thickness. Key to our study is a pressure transfer standard that is directly traceable to the National Institute of Standards and Technology’s (NIST) primary pressure standards. By comparing the pressure reported by the optomechanical sensors and transfer standard, we demonstrate optomechanical pressure measurements at accuracies competitive with high precision legacy gauges for the high vacuum range (10^{-6} Pa to 0.1 Pa), while offering calibration-free operation [9, 17, 18]. Measurements of the pressure-independent, intrinsic damping of a SiN sensor shows that its long-term baseline drift substantially outperforms our transfer standard. We can equivalently view our pressure comparisons as calibrations of the optomechanical device sensitivity, permitting optomechanical pressure sensing with lower total uncertainty. From the sensitivity measurements, we deduce the thin-film density of our devices with less than 1 % uncertainty, which may aid development of calibration-free optomechanical sensors for other physical quantities.

The remainder of the paper is structured as follows. We detail the operating principle of optomechanical pressure sensors based on mechanical damping and our methods for comparing the optomechanically measured pressure to the transfer standard in Sec. II. Our apparatus and data acquisition techniques are described in Sec. III. Section IV presents the results of our study, which we discuss in Sec. V. Appendix A describes fabrication of our silicon nitride devices. Appendix B contains uncertainty analysis for our optomechanical sensors and transfer standard.

II. THEORY OF OPERATION

Mechanical oscillators are subject to pressure-dependent damping due to collisions with ambient gas. The damping rate exhibits three regimes as a function of pressure. At sufficiently low pressures, the oscillator is in the “intrinsic damping regime”, where the gas-

^{*} Present address: Physics Department, Case Western Reserve University.

[†] daniel.barker@nist.gov

induced damping is small compared to other damping mechanisms, such as thermoelastic damping, anchor loss, or two-level systems [19]. In this regime, the total mechanical damping rate is roughly equal to the intrinsic damping rate Γ_0 , which includes all pressure-independent damping processes. At higher pressures, the oscillator enters the “molecular-flow-dominated regime”, where gas-induced damping is stronger than intrinsic damping and the total mechanical damping rate depends linearly on pressure [20–22]. At yet higher pressures, the oscillator reaches the “viscous-flow-dominated regime”, where the mean free path of the gas molecules becomes comparable to, or smaller than, the size of the oscillator and the total mechanical damping rate increases with the square root of the pressure [23, 24] [25].

We focus our efforts on measuring optomechanical pressure sensor performance in the molecular-flow-dominated regime. Our pressure transfer standard operates below 13.3 kPa, which is insufficient for a high accuracy study in the viscous-flow-dominated regime. Molecular-flow damping contributes significantly to the total damping rate at 13.3 kPa for our devices, which transition into viscous-flow-dominated operation at pressures on the order of 1000 Pa (see Sec. IV). Comparing optomechanical pressure measurements in the viscous-flow-dominated regime to a pressure standard would allow us to carefully assess the accuracy of approximations to the Navier-Stokes equations and numerical approaches to damping calculations [16, 23, 24, 26]. We plan to carry out such comparisons using another transfer standard in future work.

In molecular flow, the gas-induced damping rate can be calculated from the force noise power spectral density of the gas particle impacts using the fluctuation-dissipation theorem [21, 22]. For a thin, planar mechanical oscillator, it is given by [21, 22]

$$\Gamma_m = \frac{(1 + \pi/4)\alpha + 2(1 - \alpha)}{\rho h} \sqrt{\frac{8m_g}{\pi k_B T}} P, \quad (1)$$

where ρ is the oscillator density, h is the oscillator thickness, m_g is the molecular mass of the gas, P is the gas pressure, T is the temperature of the gas and oscillator (assumed to be in thermal equilibrium), and k_B is the Boltzmann constant. The momentum accommodation coefficient α is the fraction of gas molecules that reflect diffusely from the oscillator surface with a sensitivity pre-factor of $1 + \pi/4 \approx 1.785$ [21, 22]. The remaining fraction of the gas ($1 - \alpha$) reflects specularly with a sensitivity pre-factor of 2 [20–22]. By combining Γ_0 , Γ_m , and the viscous damping rate Γ_v , we arrive at the total mechanical damping rate [24]

$$\Gamma_t = \Gamma_0 + \frac{\Gamma_m \Gamma_v}{\Gamma_m + \Gamma_v}. \quad (2)$$

When $\Gamma_0 \ll \Gamma_m \ll \Gamma_v$, Eq. (2) simplifies to $\Gamma_t \approx \Gamma_m$, so a measurement of Γ_t yields the gas pressure through inversion of Eq. (1). Expressions analogous to Eq. (1)

for other mechanical oscillator geometries can be found using the results of Refs. [21, 22].

Equation (1) and Eq. (2) suggest that planar mechanical oscillators can act as primary (requiring no calibration from another transducer) pressure sensors [27]. Taking the molecular flow limit, $\Gamma_m \ll \Gamma_v$, the measurement equation for the pressure is

$$P = \frac{\rho h}{(1 + \pi/4)\alpha + 2(1 - \alpha)} \sqrt{\frac{\pi k_B T}{8m_g}} \Gamma'_t, \quad (3)$$

where $\Gamma'_t = \Gamma_t - \Gamma_0$ is the background-subtracted, total mechanical damping rate. Aside from the need to measure Γ_t and Γ_0 , a primary pressure measurement using Eq. (3) requires that ρ , h , and T be determined independently from P with quantified uncertainty [27]. Gases principally reflect diffusely from surfaces, so a mechanical-damping-based pressure sensor can be primary provided that its operation is consistent with $\alpha = 1$ [9, 17, 28]. We note that sensors relying on rotational damping measurements, such as spinning rotor gauges [9], suffer 100 % maximum pressure uncertainty due to $\alpha \neq 1$, whereas sensors relying on linear damping measurements, as in Eq. (3), have a maximum $\alpha \neq 1$ uncertainty of 12 %. Assessments of primary pressure sensors are typically conducted with pure gases or known mixtures [29–31]. Most pressure gauges operating in the high vacuum range incur additional uncertainty when measuring unknown gas compositions [9, 31–33], which is also the case for a pressure sensor based on Eq. (3). For typical high-vacuum contaminant gases, the sensitivity of such a pressure sensor varies by 20 % relative to N_2 , which is comparable to the sensitivity variation of ionization gauges and cold-atom sensors [31–33].

To test an optomechanical pressure sensor’s accuracy and operating pressure range, we can compute its pressure reading via Eq. (3) and compare with the reading P_{ref} of a trusted reference gauge. Such a comparison can be viewed in two equally valid ways [31]. First, we can compare the two pressure readings directly over a range of test pressures. If the reference gauge calibration is traceable to a primary standard, then the optomechanical pressure sensor is primary for the pressure range in which the readings agree within their mutual uncertainty. Practically, the comparison must use a known test gas and background subtraction, so we determine the pressure range in which

$$P'_{\text{ref}} = \frac{\rho h}{1 + \pi/4} \sqrt{\frac{\pi k_B T}{8m_g}} \Gamma'_t = P, \quad (4)$$

where $P'_{\text{ref}} = P_{\text{ref}} - P_{\text{ref},0}$ is the background-subtracted reference pressure, with $P_{\text{ref},0}$ the reference gauge reading at base pressure (when no test gas has been introduced, see Sec. III). Second, we can measure the device pressure sensitivity coefficient $S = 1/\rho h$. To perform the sensitivity measurement, we define the characteristic

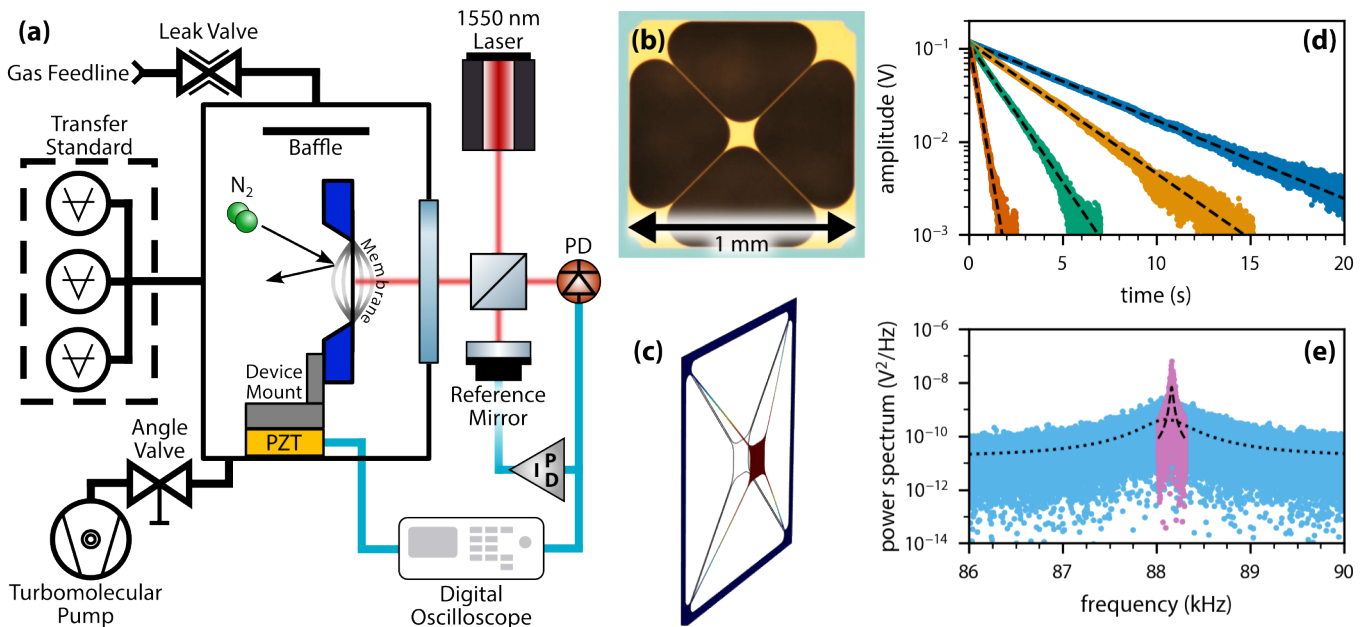


FIG. 1. (a) schematic of the experimental apparatus. The optomechanical device shown is a silicon carbide membrane. The silicon nitride trampolines are mounted similarly (see text). (b) optical microscope image of a representative trampoline similar to SiN 1. (c) simulation of the fundamental mode of an optomechanical trampoline. (d) typical mechanical ring-down signals for SiN 1. Single, Hilbert-transformed ring downs are shown at base pressure (blue), 10 mPa of Ar (yellow), 50 mPa of Ar (green), and 260 mPa of Ar (red). Black dashed curves are exponential fits to each ring-down. (e) typical thermo-mechanical noise spectra for SiN 1. Single spectra are shown at 11 Pa of Ar (pink), and 291 Pa of Ar (light blue). Black dashed and dotted curves are Lorentzian fits to the lower pressure spectrum and higher pressure spectrum, respectively.

acceleration

$$a_c = \frac{\Gamma'_t}{1 + \pi/4} \sqrt{\frac{\pi k_B T}{8m_g}} = SP'_{\text{ref}}. \quad (5)$$

If the S extracted from a linear fit to Eq. (5) agrees with the sensitivity predicted by prior characterization of ρ and h , then the pressure sensor is primary in the molecular-flow-dominated regime. One advantage of this second interpretation is that it allows us to determine the performance of the optomechanical device as both a primary and calibrated pressure gauge.

III. APPARATUS

We assess the pressure-sensing performance of optomechanical devices by placing them in a vacuum chamber whose pressure is continuously measured by a transfer standard. The main features of the apparatus are shown in Fig. 1(a). A 77 L s^{-1} turbomolecular pump evacuates the vacuum system to a base pressure, as measured by a Bayard-Alpert ionization gauge, of approximately $2 \times 10^{-5} \text{ Pa}$. We introduce ultra-high purity test gases into the vacuum chamber with a variable leak valve. We set test gas pressures below 1 Pa directly with the leak valve. To protect the turbomolecular pump, we increase the test gas pressure above 1 Pa by reducing the effective

pumping speed with an angle valve. A baffle located in front of the gas inlet ensures that the test gas thermalizes with the vacuum chamber walls before interacting with any of our pressure sensors. Two calibrated industrial platinum resistance thermometers (PRTs) measure the vacuum system temperature. The PRTs are attached to opposite sides of the vacuum chamber exterior, with one near the gas inlet and the other at the connection to the transfer standard.

The transfer standard is a suite of calibrated capacitance diaphragm gauges (CDGs). It is connected to the vacuum system by a tube with a 4.6 mm inner diameter. The CDGs are directly calibrated by NIST's oil and mercury ultrasonic interferometer manometers. We discuss the measurement uncertainties of the CDGs in Appendix B. The CDG suite is housed in an insulated enclosure that is temperature stabilized to $23.78 \text{ }^\circ\text{C}$ by an air-to-air thermoelectric heat exchanger. An out-of-loop, calibrated PRT monitors the transfer standard temperature and reports that it is stable to better than $\pm 0.01 \text{ }^\circ\text{C}$ over the duration of our measurement campaign. Further description of the transfer standard is available in Ref. [34, 35].

We measure the motion of our optomechanical devices with a homodyne Michelson interferometer (see Fig. 1). A non-polarizing beamsplitter divides light from a 1550 nm laser into a reference path and a probe path. The probe path enters the vacuum chamber and

is retroreflected by the optomechanical device under test, while the reference path is retroreflected by a mirror. The beamsplitter recombines the reflected light from the two paths onto an amplified photodiode (PD). The photodiode signal is sent to a proportional-integral controller, that stabilizes the Michelson interferometer fringe via low-frequency piezoelectric feedback to the position of the reference path mirror, and to a digital oscilloscope, which records intensity fluctuations at the mechanical resonance frequency.

We have sequentially installed four optomechanical devices in the apparatus. Two of the devices are silicon nitride trampolines fabricated at NIST [36, 37]. The first device, denoted SiN 1, has a 1 mm wide, square support frame and a photonic crystal mirror patterned into its central pad. The second device, denoted SiN 3, has a 3 mm wide, square support frame; it does not have a photonic crystal etched in its central pad. A representative silicon nitride trampoline is shown in Fig. 1(b). The fundamental mechanical modes of SiN 1 and SiN 3, see Fig. 1(c), have resonance frequencies of approximately 88 kHz and approximately 30 kHz, respectively. Further details of the silicon nitride device design and fabrication are provided in Appendix A. The last two devices are commercial silicon carbide membranes manufactured by Norcada, Inc [38]. These devices, denoted SiC 2a and SiC 2b, are 2 mm wide, square membranes. We use SiC 2a for pressure comparisons with the transfer standard and SiC 2b for Allan deviation measurements. The resonance frequency of SiC 2a's (1, 3) mode is approximately 217 kHz and that of SiC 2b's (1, 1) mode is approximately 97 kHz. The devices are attached to an in-vacuum piezoelectric shaker via either a vacuum-compatible kinematic mount (SiN 1 and SiN 3), or a custom aluminum pedestal mount (SiC 2a and SiC 2b), as shown in Fig. 1(a).

We predict the pressure sensitivity coefficient S for each device from its density and thickness. We determine the device thickness h using ellipsometry. The associated $k = 1$ standard uncertainty u_h is the standard deviation of four ellipsometer measurements at distinct points on the device frame. Devices SiN 1, SiN 3, SiC 2a, and SiC 2b have $h = 220.4(0.6)$ nm, $h = 224.2(1.3)$ nm, $h = 51.3(0.5)$ nm, and $h = 49.4(0.6)$ nm, respectively. (Here, and throughout the paper, parenthetical quantities represent $k = 1$ standard uncertainties [39], where k is the coverage factor). Silicon nitride thin films are lower density than bulk silicon nitride, so we characterize the density of our films by comparing the mass of a silicon wafer before and after deposition of a 1 μ m thick SiN layer using a calibrated scale. We estimate that the relative standard uncertainty of our device density u_ρ/ρ is 5 %, to account for potential density variation with layer thickness and from batch-to-batch. The nominal density of SiN 1 and SiN 3 is $\rho = 2810(141)$ kg m⁻³, which is consistent with other typically reported values for SiN thin film density at $k = 2$ [40–42]. The membrane of devices SiC 2a and SiC 2b is thin-film, single-

crystal 3C-SiC, which has been shown to have the same density as bulk, single-crystal silicon carbide [43, 44]. We therefore take $\rho = 3210(20)$ kg m⁻³, where the standard uncertainty is the average uncertainty of the of the thin-film 3C-SiC density measurements reported in Ref. [43]. The pressure sensitivities for each device are then $S = 1615(81)$ m kg⁻², $S = 1587(80)$ m kg⁻², $S = 6074(66)$ m kg⁻², and $S = 6310(86)$ m kg⁻² for device SiN 1, SiN 3, SiC 2a, and SiC 2b, respectively.

We measure the damping rate of our devices using mechanical ring-down and thermo-mechanical noise. For mechanical ring-down, the digital oscilloscope's integrated function generator resonantly excites the device under test using the piezoelectric shaker. When the resonant drive is removed, the excited mechanical motion “rings down”, yielding an exponentially decaying, sinusoidal oscillation of the Michelson interferometer signal. We Hilbert transform the signal to extract the envelope, which we fit to an exponential decay to measure Γ_t . Figure 1(d) shows typical Hilbert-transformed ring-downs with the associated exponential fits. For thermo-mechanical noise, we digitize the interferometer signal without applying an excitation to measure the Brownian motion of the device. We then construct the power spectrum of the mechanical motion from the signal's fast Fourier transform. A Lorentzian fit to the power spectrum at the mechanical resonance frequency then yields Γ_t . Figure 1(e) shows example spectra with Lorentzian fits.

The mechanical ring-down and thermo-mechanical noise measurements agree within their statistical uncertainty at all pressures. At low pressure, mechanical ring-down offers faster measurement repetition rates and higher signal-to-noise ratio than thermo-mechanical noise. At high pressures, the increased gas damping degrades the achievable ring-down excitation amplitude. We also begin to observe beating, presumably between our target mechanical mode and nearby modes of the device or mount, in the ring-down signal. We therefore switch from using ring-down to thermo-mechanical noise above a transition pressure of 10 Pa for devices SiN 1 and SiN 3, and of 5 Pa for device SiC 2a and SiC 2b. The different transition pressure is due to the differences in device mounting and sensitivity. The ring-down measurement uncertainty in Γ_t is comparable to that offered by the thermo-mechanical noise approach at and above the transition pressure for the silicon nitride devices. Thermo-mechanical noise measurements on the silicon carbide devices never match the uncertainty of the ring-down measurements, because the ring-down uncertainties on the silicon carbide devices are much lower than on the silicon nitride devices.

IV. RESULTS

We measure the damping response of our optomechanical sensors from approximately 10⁻⁴ Pa up to approx-

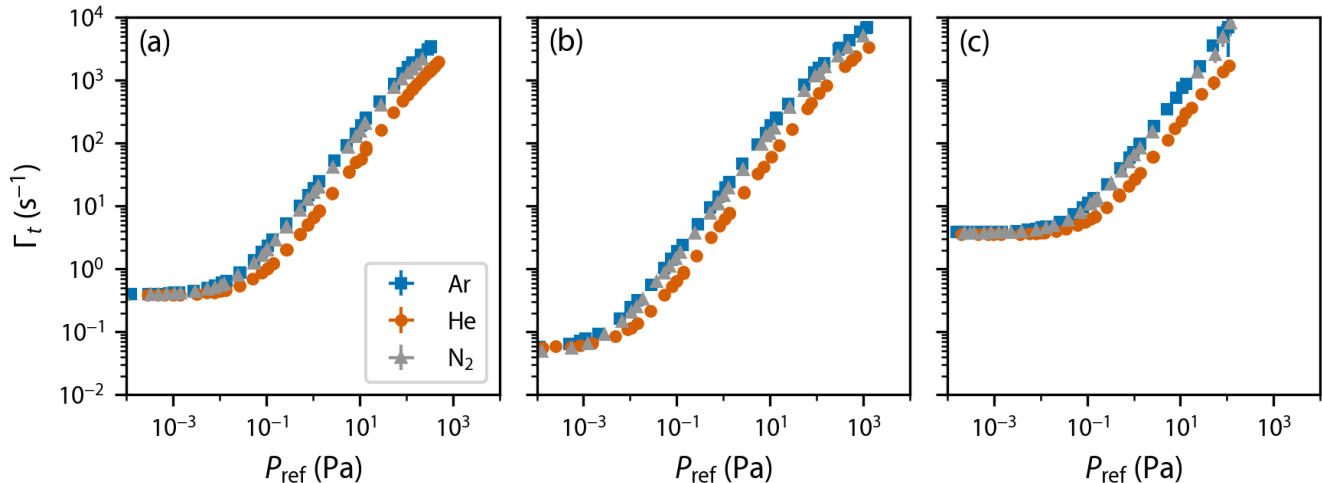


FIG. 2. Γ_t as a function of P_{ref} for device SiN 1 (a), SiN 3 (b), and SiC 2a (c). Blue squares, red circles, and gray triangles show data for Ar, He, and N_2 test gases, respectively. Horizontal and vertical error bars denote the type-A (statistical) standard uncertainty at coverage factor $k = 1$ (most error bars are smaller than the data points).

imately 1 kPa. Figure 2 shows Γ_t for each sensor as a function of P_{ref} for three test gases: Ar, He, and N_2 . At low pressure, Γ_0 makes the largest contribution to Γ_t . At intermediate pressure, the molecular flow damping exceeds Γ_0 and the sensors exhibit a linear damping response to pressure. At high pressure, the gas enters viscous flow and Γ_t transitions toward a square root dependence on pressure. The onset of viscous flow is more apparent for the silicon nitride sensors and less clear for the silicon carbide sensor. The higher sensitivity of the silicon carbide sensor and the signal-to-noise ratio of the interferometer limit how far into the viscous flow regime we can measure the response of SiC 2a.

A. Primary Operation

We assess each device's performance as a pressure sensor by comparing its pressure reading to the transfer standard. We background subtract both the damping rate and the transfer standard pressure to eliminate contributions from residual gases and intrinsic damping. We then convert Γ'_t to P using Eq. 4. The optomechanical pressure P and transfer standard pressure P'_{ref} are plotted against each other in the upper row of Figure 3. In molecular flow, the optomechanical sensor and transfer standard readings collapse toward a line with unit slope. The error bars in the upper row of Fig. 3, most of which are smaller than the data points, represent the total (statistical and non-statistical) $k = 1$ standard uncertainty in both the optomechanical sensor and the transfer standard (see Appendix B for a full uncertainty analysis). The agreement between the sensor and standard is easier to discern through the percent difference $\Delta\% = 100 \times (1 - P/P'_{\text{ref}})$, which is shown for each op-

tomechanical sensor in the lower row of Fig. 3. The uncertainty in $\Delta\%$ is propagated from both P and P'_{ref} (*i.e.* horizontal error bars in the upper row of Fig. 3 are incorporated into the vertical error bars in the lower row).

For the heavy gases Ar and N_2 , all optomechanical sensors agree with the transfer standard within the mutual uncertainty in the molecular flow regime. Crucially, the agreement between optomechanical sensor and transfer standard occurs under the assumption that $\alpha = 1$, indicating that our devices are primary pressure sensors. The useful operating range for the optomechanical sensors extends roughly from 10^{-2} Pa to 10 Pa, depending on the sensor. The lower limit of the operating range is the pressure at which the statistical uncertainty in Γ'_t , given by the quadrature sum of the statistical uncertainties in Γ_t and Γ_0 , becomes comparable to the uncertainty in S . The upper limit of the operating range is set by the transition into viscous flow. Within the operating range, the total uncertainty of the optomechanical sensor is dominated by statistical uncertainty in Γ'_t and uncertainty in the device sensitivity $S = 1/\rho h$. Combining these two uncertainties in quadrature, we find that device {SiN 1, SiN 3, SiC 2a} is accurate to {5.3 %, 6.1 %, 1.1 %} of reading for ring-down measurements in its operating range. The accuracy of SiC 2a is competitive with high performance gauges operating in this pressure range and suggests that silicon nitride devices could achieve similar accuracy with better characterization of ρ (*e.g.*, Rutherford backscattering [40, 41]), since, for SiN 1 and SiN 3, $u_\rho/\rho = 5$ % dominates the total measurement uncertainty estimated above.

The optomechanical sensors report a higher pressure for He than for Ar or N_2 . Across all our sensors, the increase in reported He pressure is roughly 3 % in the useful operating range. For SiN 1 and SiN 3, the He

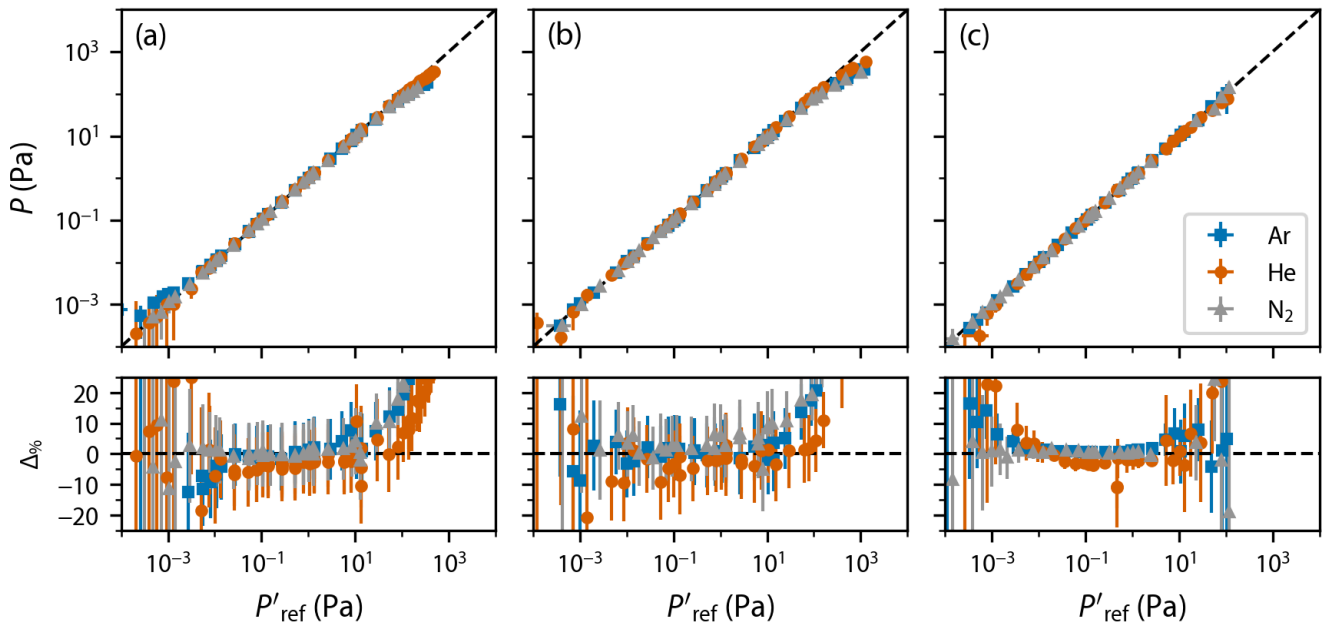


FIG. 3. Pressure sensing performance of device SiN 1 (a), SiN 3 (b), and SiC 2a (c). In each subplot, the upper row shows P as a function of P'_{ref} and the lower row shows the percent difference $\Delta\%$ between the two pressures. Blue squares, red circles, and gray triangles show data for Ar, He, and N_2 test gases, respectively. Black dashed lines are a guide to the eye indicating perfect agreement between the optomechanical sensor and transfer standard. Horizontal and vertical error bars denote the total (statistical and non-statistical) standard uncertainty at $k = 1$. In the upper row, most error bars are smaller than the data points.

pressure still agrees with the transfer standard within the mutual uncertainty (see Fig. 3 lower row). However, while it is not immediately apparent in Fig. 3(c), the He pressure measured by SiC 2a disagrees with the transfer standard by more than twice the total standard uncertainty. There are two likely explanations for the shift in the He measurements. First, He is significantly more sensitive to impurities in the test gas due to its low mass; an approximately 1 % N_2 contamination of the gas feedline would produce a shift of similar size. However, we have extensively tested the gas feed system and see no evidence of contamination or outgassing at the necessary level (see Appendix B 2). Second, specular reflections could contribute significantly to the damping due to helium's large thermal de Broglie wavelength. A momentum accommodation coefficient for He scattering of $\alpha_{\text{He}} \approx 0.75$ would explain the shift from the measurements with heavier gases. A lower momentum accommodation for He is consistent with the observation of increasing thermal accommodation with gas mass reported in Refs. [45, 46]. Our observation of imperfect momentum accommodation suggests that optomechanical pressure sensors may require calibration to sense the pressure of light gases with 1 % fractional accuracy.

The utility of any gauge depends critically on its stability and baseline drift. We characterize the former using the fractional Allan deviation of Γ_t , which is shown as a function of averaging time τ in Figure 4 for ring-down

measurements on devices SiN 3 and SiC 2b. Initially, the Allan deviation decreases with $\sqrt{\tau}$, as expected for white-noise-limited measurements. At base pressure, the Allan deviation for SiC 2b decreases throughout the 3000 s averaging time and the Allan deviation for SiN 3 turns upward after approximately 5000 s of averaging. When we inject N_2 test gas, the Allan deviation turns upward after approximately 100 s to 1000 s of averaging. We suspect that the instability for the N_2 measurements is due to fluctuations of the leak valve conductance, which is supported by the behavior of the Allan deviation of the transfer standard. The higher Allan deviation for SiN 3 is likely due to its lower sensitivity leading to longer ring-down times and lower resonance frequency leading to increased acoustic noise in the interferometer. At all pressures in Fig. 4, both SiN 3 and SiC 2b attain statistical uncertainties significantly below those of the comparison of Fig. 3, which were achieved in a measurement time of approximately 10 s in the molecular-flow-dominated regime. Therefore, we believe that the useful operating range of our sensors can be extended to lower pressure at the expense of measurement time and that SiN 3 and SiC 2b can resolve fractional pressure differences less than 1 % and 0.1 %, respectively. Figure 4(a) further supports our supposition that silicon nitride devices can achieve total uncertainty comparable with silicon carbide devices using a lower uncertainty measurement of ρ .

The baseline drift of our optomechanical sensors is

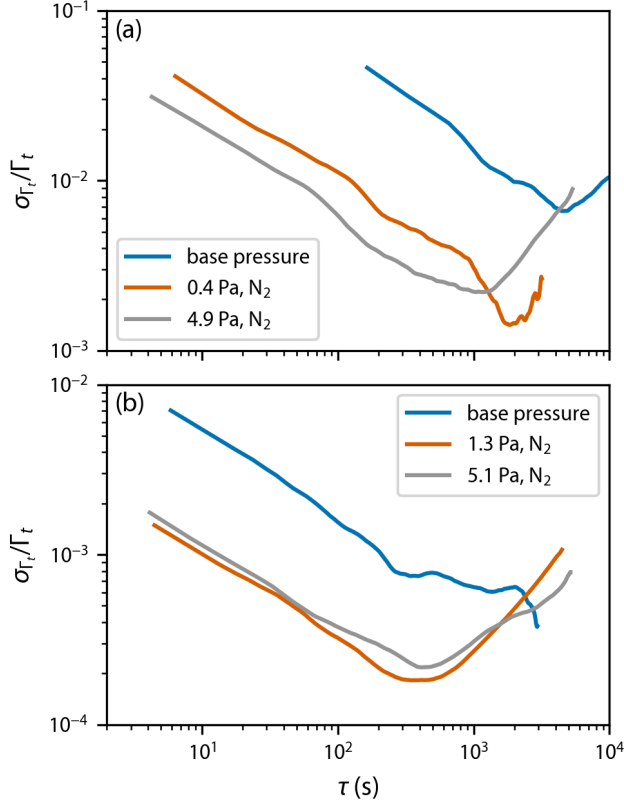


FIG. 4. Fractional Allan deviation $\sigma_{\Gamma_t}/\Gamma_t$ as a function of averaging time τ for SiN 3 (a) and SiC 2b (b). The blue curve in each subplot shows data taken at base pressure, while the red and gray curves show data for two pressures of N_2 test gas.

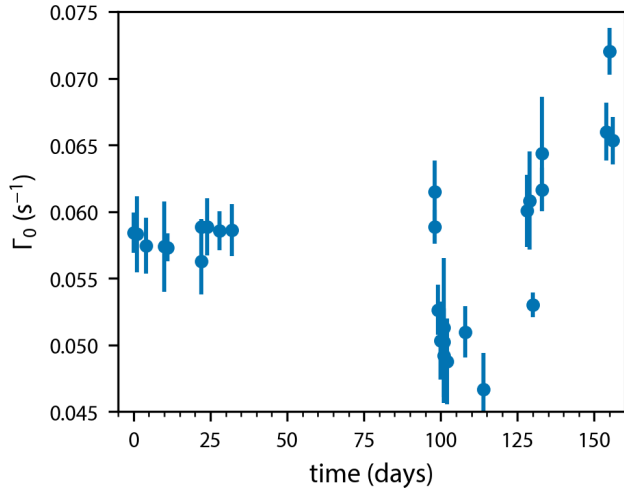


FIG. 5. Intrinsic damping Γ_0 as a function of measurement day. Error bars represent the statistical uncertainty of 5 repeated measurements.

lower than the pressure drift of the transfer standard. We evaluate the baseline drift in our optomechanical sensors by repeatedly measuring their damping rate at base pressure. Figure 5 shows Γ_0 for SiN 3 as a function of the time in days since the beginning of our measurement campaign (the baseline drift of SiN 1 and SiC 2a were evaluated over shorter time intervals, see Appendix B 1). During the large gap in the data, from roughly day 35 to day 95, SiN 3 was removed from the vacuum chamber and held at atmospheric pressure. On a day-to-day basis, nearly all successive Γ_0 measurements agree within their mutual uncertainty. The drift per day between successive measurements has a inverse-variance-weighted average of $7(6) \times 10^{-5} \text{ s}^{-1}/\text{d}$ and an unweighted average magnitude of $2.6(9) \times 10^{-3} \text{ s}^{-1}/\text{d}$. Excluding the data from day 99 to day 115, which we acquired during a period of extended air-conditioning system maintenance, the inverse-variance-weighted average drift per day becomes $5(5) \times 10^{-5} \text{ s}^{-1}/\text{d}$ and the unweighted average magnitude becomes $2.7(1.1) \times 10^{-3} \text{ s}^{-1}/\text{d}$. The most conservative drift estimate above is equivalent to an N_2 pressure drift at 20 °C of approximately 180 $\mu\text{Pa}/\text{d}$, more than 10 times lower than the pressure drift of the transfer standard, which illustrates the potential for high stability pressure sensing with optomechanical devices.

B. Quantitative Comparison

Accurately quantifying the agreement between the pressures reported by the optomechanical sensors and the transfer standard is challenging because uncertainty in S is perfectly correlated across all data points. We approach the problem by re-framing our comparison as a measurement of S . We compute the characteristic acceleration a_c (see Eq. (5)) for each {sensor, test gas} pair, which depends linearly on P'_{ref} in the molecular flow regime. The measured sensitivity S_m is given by the slope of a linear fit to the data. If S_m and predicted sensitivity S agree within their mutual uncertainty then the optomechanical sensor is primary (see Sec. II and Sec. III).

We perform the linear fit using maximum likelihood estimation on the orthogonal distance. When parameterized by the slope S_m and intercept b , the orthogonal distance of the i th data point ($P'_{\text{ref},i}, a_{c,i}$) from a line is $d_i = a_{c,i} - S_m P'_{\text{ref},i} - b$. The log-likelihood for the orthogonal distance is

$$\ln \mathcal{L} = \frac{1}{2} \ln \left(\det \left(C(\vec{a}_c) + S_m^2 C(\vec{P}'_{\text{ref}}) \right)^{-1} \right) + \frac{1}{2} \vec{d}^T \left(C(\vec{a}_c) + S_m^2 C(\vec{P}'_{\text{ref}}) \right)^{-1} \vec{d}, \quad (6)$$

where $C(\vec{a}_c)$ and $C(\vec{P}'_{\text{ref}})$ are the covariance matrices for the set of measurements \vec{a}_c and \vec{P}'_{ref} , respectively. We note that the covariance matrices are not diagonal (see Appendix B). To ensure that we are not fitting

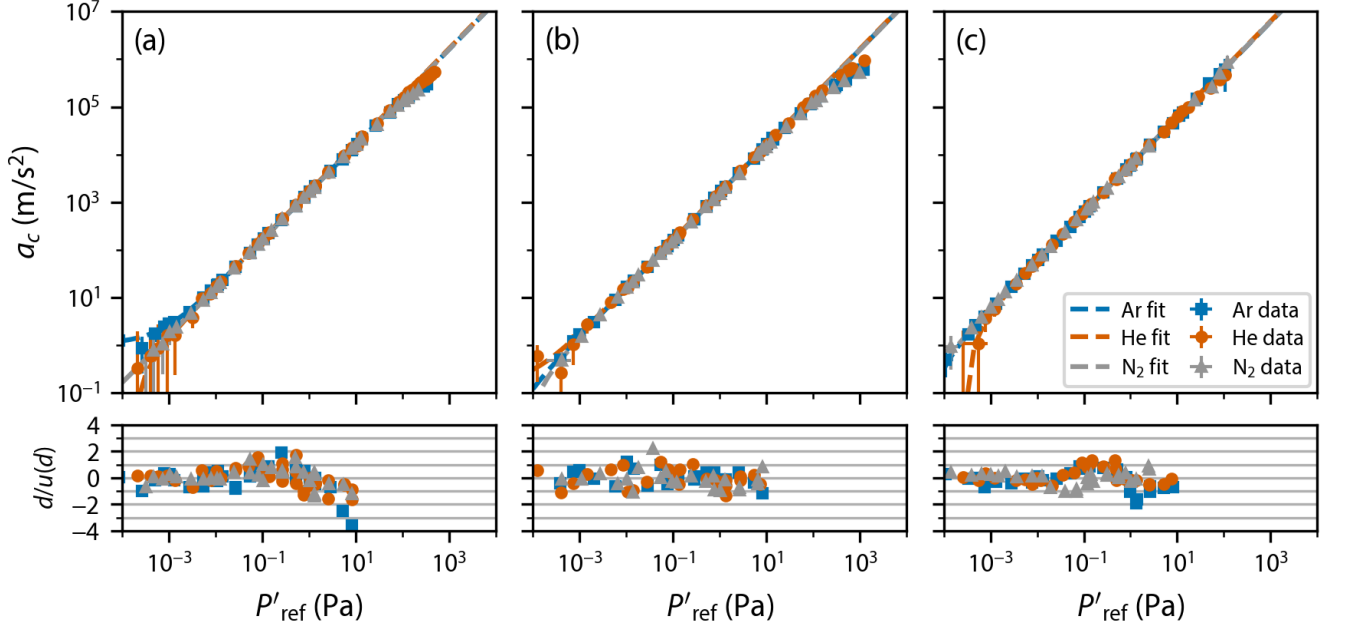


FIG. 6. Characteristic acceleration a_c as a function of P'_{ref} for SiN 1 (a), SiN 3 (b), and SiC 2a (c). Blue squares, red circles, and gray triangles in the upper row of each subplot show data for Ar, He, and N_2 test gases, respectively. The correspondingly colored dashed lines are maximum likelihood fits to the data. Horizontal and vertical error bars denote the total (statistical and non-statistical) standard uncertainty at $k = 1$. The lower row of each subplot shows the fit residuals normalized to the total standard uncertainty in the orthogonal distance with colored symbols corresponding to the data in the upper row.

into the viscous flow regime, we include data up to a variable cut-off pressure $P'_{\text{ref, cut}}$ in our minimization of Eq. (6) and observe that S_m is independent of $P'_{\text{ref, cut}}$ for $P'_{\text{ref, cut}} \lesssim 100$ Pa. Figure 6 reports the maximum likelihood fit results with $P'_{\text{ref, cut}} = 10$ Pa, chosen well below the onset of viscous flow, for each test gas and sensor. The lower row in each subplot shows the fit residuals d_i normalized to the total $k = 1$ standard uncertainty in the orthogonal distance $u(d_i) = \sqrt{u^2(a_{c,i}) + S_m^2 u^2(P'_{\text{ref},i})}$, where $u(a_{c,i})$ and $u(P'_{\text{ref},i})$ are the standard uncertainties in the i th measurement of a_c and P'_{ref} , respectively.

The fit residuals for our three optomechanical sensors are quite different, depending on the dominant sources of uncertainty in the data. Device SiN 3 is limited by statistical uncertainty in Γ'_t , so its residuals appear unstructured (see Appendix B 1). Non-statistical uncertainties in the transfer standard contribute more significantly for SiN 1 and SiC 2a, which have lower statistical Γ'_t uncertainty. As a result, correlations begin to appear in the fit residuals for these two devices. We believe these small correlations arise from drifts in the transfer standard calibration and base pressure reading (see Appendix B 2). We also assess the fit quality using $\chi^2_\nu = \chi^2/\nu$, where ν is the number of degrees of freedom in the fit and we include the correlated uncertainties in our calculation of χ^2 following Ref. [47]. We find $\chi^2_\nu = 1.01$ for {SiN 1, Ar} ($\nu = 30$), $\chi^2_\nu = 0.80$ for {SiN 1, He} ($\nu = 39$), $\chi^2_\nu = 0.59$ for {SiN 1, N_2 } ($\nu = 30$), $\chi^2_\nu = 0.34$ for {SiN 3, Ar}

($\nu = 21$), $\chi^2_\nu = 0.59$ for {SiN 3, He} ($\nu = 23$), $\chi^2_\nu = 0.57$ for {SiN 3, N_2 } ($\nu = 21$), $\chi^2_\nu = 0.84$ for {SiC 2a, Ar} ($\nu = 25$), $\chi^2_\nu = 0.86$ for {SiC 2a, He} ($\nu = 26$), and $\chi^2_\nu = 0.86$ for {SiC 2a, N_2 } ($\nu = 26$). All fits pass the χ^2 test, where the probability of observing a χ^2_ν at least as large as those above exceeds 5 % [48].

We determine the uncertainty in the maximum likelihood fit parameters S_m and b using a Markov chain Monte Carlo (MCMC) method. Markov chain Monte Carlo allows our parameter uncertainty estimation to include the correlated uncertainties in our measurements. We implement the MCMC using the `emcee` Python package [49]. The fitted intercept b agrees with 0 m/s^2 at $k = 2$ for all devices and gases, except for SiN 1 with Ar, where it agrees at $k = 3$. Table I shows S_m and S along with their degree of equivalence

$$E(S) = \frac{S - S_m}{2u(S - S_m)} \quad (7)$$

for each sensor and test gas, where $u(S - S_m) = \sqrt{u^2(S) + u^2(S_m)}$ is the uncertainty in the difference of the measured and predicted sensitivities. All measured and predicted sensitivities agree at $k = 2$, except the {SiC 2a, He} combination, which agrees at $k = 3$. Additionally, the measured Ar and N_2 sensitivities for each device agree with each other at $k = 2$. Together, the two results above confirm that our sensors are accurate to within the uncertainties quoted in the discussion of Fig. 3 for heavy gases. The measured He sensitivity is

TABLE I. Measured and predicted sensitivities for all devices and gases. The table also shows the device density ρ_m extracted from the sensitivity measurement. Parenthetical quantities represent total (statistical and non-statistical) $k = 1$ standard uncertainties.

Device	Gas	S_m (m ² /kg)	S (m ² /kg)	$E(S)$	ρ_m (kg/m ³)
SiN 1	Ar	1602(7)	1615(81)	0.08	2832(14)
	He	1667(4)	1615(81)	-0.32	2722(10)
	N ₂	1607(5)	1615(81)	0.05	2824(12)
SiN 3	Ar	1578(11)	1587(80)	0.06	2826(26)
	He	1628(14)	1587(80)	-0.25	2740(28)
	N ₂	1555(11)	1587(80)	0.20	2868(26)
SiC 2a	Ar	6030(11)	6074(66)	0.33	3233(29)
	He	6237(13)	6074(66)	-1.21	3127(28)
	N ₂	6058(11)	6074(66)	0.12	3219(29)

higher than the measured heavy gas sensitivities by approximately 3.4 % (averaged over all devices), consistent with $\alpha \approx 0.75$.

Using the measured sensitivities, we can operate our devices as calibrated, rather than primary, pressure sensors. We extract average S_m for Ar and N₂ to a fractional uncertainty of {0.4 %, 0.7 %, 0.18 %} for sensor {SiN 1, SiN 3, SiC 2a}. When combined with the statistical uncertainty in the operating range demonstrated in Fig. 3, sensor {SiN 1, SiN 3, SiC 2a} is accurate to {1.8 %, 3.6 %, 0.3 %} of reading for calibrated measurements. The calibrated accuracy of SiC 2a approaches or exceeds that of other high performance gauges operating in the same pressure range, such as CDGs and spinning rotor gauges.

Our approach allows density measurements of thin-film devices that surpass Rutherford backscattering spectroscopy. By combining S_m with the ellipsometer measurements of h , we determine the *in situ* density of our devices ρ_m . Table I shows the ρ_m obtained for each device and test gas. The total fractional uncertainty in ρ_m for SiN is less than 1 %, which is substantially lower than the uncertainties reported for Rutherford backscattering spectroscopy in Refs. [40, 41]. Our method of measuring the mechanical damping as a function of pressure can be a useful complementary technique for characterizing the density of SiN thin films.

V. CONCLUSION

We have carefully explored the performance and limitations of optomechanical pressure sensors. By comparing damping-based pressure measurements from three optomechanical devices to a transfer standard, we confirm that optomechanical pressure sensors are primary in the molecular flow regime. Our sensors achieve a total measurement uncertainty less than 7 % over three decades of pressure. Owing to its fabrication from a single-crystal material, the SiC membrane sensor exhibits

a total uncertainty of 1.1 %, which, to our knowledge, is the lowest reported for an optomechanical pressure sensor. The useful operating range of optomechanical sensors can be extended with thinner, higher-sensitivity devices or device designs with less intrinsic damping, such as Refs. [16, 37, 50, 51]. Exploiting squeezed-film effects may allow primary ultra-high vacuum (10^{-9} Pa $<$ $P <$ 10^{-6} Pa) sensing, once the accuracy of squeezed-film models is verified [8, 16].

Our optomechanical sensors possess exceptional short-term and long-term stability. The Allan deviation of a SiN trampoline and a SiC membrane indicate that these sensors can reach precision better than 1 % and 0.1 %, respectively. The long-term baseline drift of our SiN trampolines is 10 times better than that of our transfer standard. If we view our pressure comparisons as a calibration of the optomechanical pressure sensitivity, we find that our sensors can deliver 0.3 % of reading accuracy. The sensitivity measurements allow us to determine the thin-film density of our SiN sensors with better than 1 % uncertainty. Such precise measurements of optomechanical damping as a function of pressure can characterize the density of other optomechanical sensors, which must have a well-known mass to achieve accurate measurements. Together, our results indicate that optomechanical pressure sensors can meet or exceed the performance of capacitance diaphragm and spinning rotor gauges.

Deploying optomechanical devices as pressure sensors in the field requires several additional advances. First, the sensor thickness and density must be stable over a timescale of years, for useful primary or calibrated operation. We have observed that the sensitivities of our sensors are stable over the duration of our measurement campaign, but longer term study is necessary. Second, the sensors should endure repeated exposure to condensable, reactive gases, which are the norm in industrial environments. High-accuracy, industrial gauges are typically heated to prevent condensation [52], but heating an optomechanical sensor may degrade its intrinsic damping and thus operating range. Third, a deployable instrument should be built using a rugged, fiber-optic Michelson interferometer. We plan to investigate the sensitivity stability and resilience of our sensors, as well as their performance using a fiber-optic interferometer, in the future.

ACKNOWLEDGEMENTS

We thank E. Norrgard and A. Chijioke for their careful reading of the manuscript. We also thank S. Eckel, J. Prothero, and J. Ricker for experimental assistance, as well as A. Migdall and I. Spielman for loaning us equipment used in this work. Our work is funded by the National Institute of Standards and Technology.

Appendix A: Trampoline Fabrication

The trampoline membranes were fabricated using a two-sided process. Silicon nitride film was deposited on the silicon substrate (525 μm thick) using low-pressure chemical vapor deposition (LPCVD). The trampolines were patterned on the front side using direct laser writing lithography and transferred into the silicon nitride through reactive ion etching (RIE). A low-temperature silicon oxide (LTO) film was then deposited as the protection layer for the subsequent steps. In order to fully release the silicon nitride trampoline membrane, the back-side of the silicon wafer was patterned with square openings using direct laser writing lithography. A combination of RIE and deep reactive ion etching (DRIE) was used to etch the pattern into silicon substrate to within 40 μm of the front surface. After the substrate was diced and cleaned, the trampoline membranes were fully released using a timed chip-by-chip etch in KOH.

Appendix B: Uncertainty Analysis

The uncertainties reported in Sec. IV are computed using the full covariance matrix for both the transfer standard and optomechanical sensor. We perform our analysis using the covariance matrix because many of the type B (non-statistical) uncertainties of the transfer standard are correlated. The total uncertainty in a set of measurements \vec{X} of a physical quantity X is described by the covariance matrix $C(\vec{X})$ with elements

$$C(X_i, X_j) = \sum_Y C_Y(X_i, X_j), \quad (\text{B1})$$

where integers i and j index the measurements of X , Y labels a source of uncertainty, and we take uncertainties due to distinct sources Y to be uncorrelated, which is the case for the significant uncertainty sources in our measurements. The uncertainty in the set of measurements \vec{X} due to source Y is given by

$$C_Y(X_i, X_j) = u_Y(X_i)u_Y(X_j)r_Y(X_i, X_j), \quad (\text{B2})$$

where $u_Y(X_i)$ is the $k = 1$ standard uncertainty in the i th measurement of X (*i.e.*, X_i) due to source Y and $r_Y(X_i, X_j)$ is the correlation coefficient between the i th and j th measurements. The main results of Sec. IV use background subtraction, which introduces additional correlations into the covariance matrices. Specifically, the elements of the covariance matrix for $\vec{X}' = \vec{X} - X_0$ due to source Y are

$$C_Y(X'_i, X'_j) = C_Y(X_i, X_j) + (u_Y(X_0))^2 - C_Y(X_i, X_0) - C_Y(X_0, X_j). \quad (\text{B3})$$

Importantly, background subtraction significantly suppresses highly correlated sources of uncertainty in the transfer standard.

We show example uncertainty budgets for the Ar test gas measurements of each device in Fig. 7. The only difference between the uncertainty budget for the direct pressure comparison (*i.e.*, P vs. P'_{ref} , see Fig. 3) and for the device sensitivity measurement (*i.e.*, a_c vs. P'_{ref} , see Fig. 6) is that uncertainties due to h and ρ do not contribute for the device sensitivity budget (see Eq. (5)). Because the fractional uncertainties in P and a_c due to source Y are the same, we choose to label all uncertainties of the optomechanical devices with physical quantity P , rather than physical quantity a_c . Blue and purple lines in Fig. 7 show the fractional $k = 1$ standard uncertainty associated with each uncertainty source for the transfer standard and optomechanical sensor, respectively. The fractional standard uncertainties are computed from the diagonal elements of the background-subtracted covariance matrix (see Eq. B3) as $u_Y(X'_i)/X'_i = \sqrt{(u_Y(X_i))^2 + (u_Y(X_0))^2 - 2C_Y(X_i, X_0)}/X'_i$. We detail the construction of the covariance matrix, Eq. (B2), for each uncertainty component below.

1. Optomechanical Sensor

The P and a_c measurements of the optomechanical sensors have eight and six sources of uncertainty, respectively. The uncertainty sources common to both measurements are the statistical uncertainty in Γ_t (and Γ_0), long-term drift uncertainty in Γ_0 , uncertainty in the gas temperature T , uncertainty in the gas composition, uncertainty in the digital oscilloscope timebase, and uncertainty in the linearity of the Michelson interferometer. As we explore below, the last three sources of uncertainty are negligible compared to the first three sources. Additionally, the pressure measurements must include uncertainty in the sensor density ρ and thickness h .

First, the statistical uncertainty in P is given by

$$C_{\text{rdm}}(P_i, P_j) = \frac{\partial P_i}{\partial \Gamma_{t,i}} u_{\text{rdm}}(\Gamma_{t,i}) \frac{\partial P_j}{\partial \Gamma_{t,j}} u_{\text{rdm}}(\Gamma_{t,j}) \delta_{ij}, \quad (\text{B4})$$

where δ_{ij} is the Kronecker delta. The uncertainty in individual exponential fits (for ring-down measurements) or Lorentzian fits (for thermo-mechanical noise measurements) is negligible compared to the spread of repeated Γ_t measurements. We therefore take the standard deviation of five repeated measurements as $u_{\text{rdm}}(\Gamma_{t,i})$. We chose to index our measurements such that $\Gamma_{t,0}$ is measured at base pressure (*i.e.* $\Gamma_{t,0} \equiv \Gamma_0$), so Eq. (B4) includes the statistical uncertainty in Γ_0 .

Second, there is uncertainty in P due to long-term drift in Γ_0 . We measure the base pressure damping rate Γ_0 for each device at the beginning of each measurement run. For devices SiN 1 and SiN 3, the average daily drift in Γ_0 is negligible compared the statistical uncertainty of the individual Γ_0 measurements (see Fig. 5). A measurement run takes approximately 8 h, so we do not include drift uncertainty in the uncertainty budget SiN 1 or SiN 3.

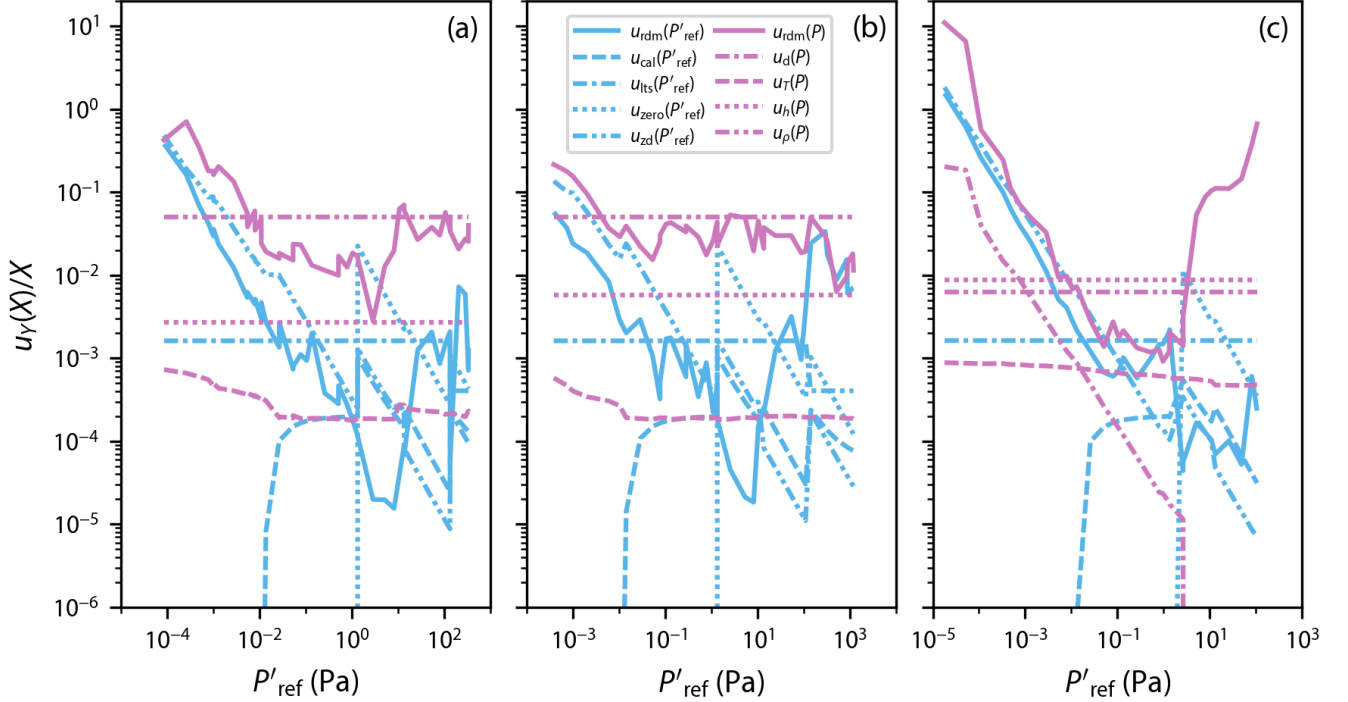


FIG. 7. Example uncertainty budget for Ar test gas measurements with SiN 1 (a), SiN 3 (b), and SiC 2a (c). Blue and purple colored curves show the fractional standard uncertainty due to each source affecting the transfer standard and optomechanical sensor, respectively. The standard uncertainties are given by the diagonal elements of the background-subtracted covariance matrices for each uncertainty component (see text).

For SiC 2a, we observe an average daily drift in Γ_0 of $B_\Gamma = 0.03 \text{ s}^{-1}/\text{d}$, which is, relative to the statistical uncertainty, significant for ring-down data and negligible for thermo-mechanical noise data. The covariance matrix for the drift is

$$\begin{aligned} C_d(P_i, P_j) &= \frac{\partial P_i}{\partial \Gamma_{t,i}} u_d(\Gamma_{t,i}) \frac{\partial P_j}{\partial \Gamma_{t,j}} u_d(\Gamma_{t,j}) \delta_{ij} \\ &= \frac{\partial P_i}{\partial \Gamma_{t,i}} B_\Gamma (t_i - t_0) \frac{\partial P_j}{\partial \Gamma_{t,j}} B_\Gamma (t_j - t_0) \delta_{ij}, \end{aligned} \quad (\text{B5})$$

where t_i is the time of the i th measurement and t_0 is the time of the first measurement of the run.

Third, there is uncertainty in the gas temperature. The two PRTs monitoring the vacuum chamber temperature report an approximately 1 K temperature gradient across the chamber. The gradient decreases with gas pressure, presumably due to the thermal conductivity of the gas, to approximately 200 mK at 1000 Pa. The PRTs have a calibration uncertainty of approximately 1 mK, which is negligible compared to the gradient. We therefore take the temperature gradient as the standard uncertainty in the gas temperature with covariance matrix

$$\begin{aligned} C_T(P_i, P_j) &= u_T(P_i) u_T(P_j) \delta_{ij} \\ &= \frac{\partial P_i}{\partial T_i} \Delta T_i \frac{\partial P_j}{\partial T_j} \Delta T_j \delta_{ij}, \end{aligned} \quad (\text{B6})$$

where ΔT_i is the temperature gradient during the i th measurement.

Fourth, there is uncertainty in the gas composition. Strictly, the mass that enters Eq. (3) is the average molecular mass $m_{\text{avg}} = \sum_g P_g m_g / \sum_g P_g$, where P_g is the partial pressure of gas g and the sum runs over all gases in the vacuum chamber [13, 15]. Background subtraction removes uncertainty due to the residual gases at base pressure, whose partial pressures do not vary during a measurement run. We have verified that there are no leaks in the gas feedline and that its outgassing is insignificant using a residual gas analyzer. Because we use ultra-high purity test gases, any mass uncertainty will contribute negligibly to the uncertainty budget.

Fifth, there is uncertainty in the timebase of the digital oscilloscope. Given the age and specifications of the oscilloscope, the timebase uncertainty is at most 10 $\mu\text{s}/\text{s}$. When propagated through Γ_t to P , the timebase uncertainty then causes 10 $\mu\text{Pa}/\text{Pa}$ fractional pressure uncertainty, which is negligible (see Fig. 7).

Sixth, there is uncertainty in the linearity of the Michelson interferometer. We stabilize the interferometer so that its intensity response to small displacements of the optomechanical sensor is approximately linear, but small deviations from linearity could distort exponential mechanical ring-downs. Given the amplitude of the interferometer's full sinusoidal intensity response to dis-

placement and our ring-down excitation amplitude, we estimate that the non-linearity is less than 0.17 %. To ensure that such a small non-linearity is not biasing our ring-down measurements, we introduce a variable photodiode voltage cutoff and only perform the ring-down exponential fit on data lying below the cutoff. We observe no systematic shift in Γ_t as a function of the voltage cutoff, indicating that interferometer non-linearity does not bias our measurements toward lower damping rates. (The amplitude of the thermo-mechanical noise is significantly lower than that of the ring-down excitation, so any non-linearity is insignificant).

Finally, there is uncertainty in P due to both ρ and h . The covariance matrices for these two sources of uncertainty are

$$C_\rho(P_i, P_j) = \frac{\partial P_i}{\partial \rho} u_\rho \frac{\partial P_j}{\partial \rho} u_\rho, \quad (\text{B7})$$

and

$$C_h(P_i, P_j) = \frac{\partial P_i}{\partial h} u_h \frac{\partial P_j}{\partial h} u_h, \quad (\text{B8})$$

respectively. We note that $C_\rho(P_i, P_j)$ and $C_h(P_i, P_j)$ do not depend on i or j , so they are perfectly correlated over P . Our assessments of u_ρ and u_h are described in Sec. III.

2. Transfer Standard

The P_{ref} measurements of the transfer standard have seven sources of uncertainty. Five uncertainty sources contribute non-negligibly to the total uncertainty of our measurements: statistical uncertainty, uncertainty of the initial calibration, uncertainty due to long-term calibration drift, uncertainty in determining the zero pressure reading, and uncertainty due to drift in the zero pressure reading. The latter two uncertainty sources arise because CDGs are fundamentally differential gauges that employ a passively pumped reference vacuum on one side of the gauge diaphragm to measure absolute pressure on the other side. Mechanical aging and temperature changes then lead to variation in the CDG “zero”, which is the indicated pressure when the absolute pressure is below the gauge’s resolution [10, 34]. There are two sources of uncertainty that do not contribute significantly to our measurements: uncertainty in the calibration of the digital multimeter (DMM) that records CDG measurements, and uncertainty in the thermal transpiration correction to the CDG readings. We describe our construction of the covariance matrix for each uncertainty source below.

First, the random statistical uncertainty has

$$C_{\text{rdm}}(P_{\text{ref},i}, P_{\text{ref},j}) = u_{\text{rdm}}(P_{\text{ref},i}) u_{\text{rdm}}(P_{\text{ref},j}) \delta_{ij}, \quad (\text{B9})$$

where we take $u_{\text{rdm}}(P_{\text{ref},i})$ to be the standard deviation of 10 repeated measurements and δ_{ij} is the Kronecker delta.

Second, we consider the uncertainty in the initial calibration of each CDG within the transfer standard by the NIST primary standards. Because each CDG has three independently calibrated gain settings, the calibration uncertainty is perfectly correlated for each {CDG, gain} pair (and uncorrelated between pairs), so

$$C_{\text{cal}}(P_{\text{ref},i}, P_{\text{ref},j}) = u_{\text{cal}}(P_{\text{ref},i}) u_{\text{cal}}(P_{\text{ref},j}) \delta_{k_i k_j} \delta_{l_i l_j}, \quad (\text{B10})$$

where k_i (l_i) indexes the CDG (gain setting) for $P_{\text{ref},i}$. The transfer standard’s calibration report provides $u_{\text{cal}}(P_{\text{ref}})$ for each CDG and gain setting. For a given CDG and gain setting, $u_{\text{cal}}(P_{\text{ref}})$ is approximately constant over the calibration pressure range and we account for its small increase with P_{ref} with linear interpolation.

Third, we describe the uncertainty associated with long-term drift of the transfer standard calibration. The calibration report provides the average fractional calibration shift between successive calibrations for each CDG in the transfer standard. The reported calibration shift is averaged over gain settings, so the covariance matrix for the long-term stability uncertainty is

$$C_{\text{lts}}(P_{\text{ref},i}, P_{\text{ref},j}) = u_{\text{lts}}(P_{\text{ref},i}) u_{\text{lts}}(P_{\text{ref},j}) \delta_{k_i k_j} \quad (\text{B11}) \\ = A_{k_i} P_{\text{ref},i} A_{k_j} P_{\text{ref},j} \delta_{k_i k_j},$$

where A_{k_i} is the fractional calibration shift coefficient for CDG k_i , averaged over the 27 year calibration history of the transfer standard.

Fourth, we include uncertainty in the initial determination of each CDG zero. We zero each {CDG, gain} pair by recording the reading at the chamber base pressure before beginning a pressure measurement run. We use the average of 10 repeated measurements as the zero reading, which is subtracted from all subsequent pressure readings (until the transfer standard is zeroed again before the next measurement run). We take the standard uncertainty of the zero $u_{\text{zero}}(k_i, l_i)$ to be the standard deviation of the 10 measurements. The covariance matrix for the initial zero uncertainty is then

$$C_{\text{zero}}(P_{\text{ref},i}, P_{\text{ref},j}) = u_{\text{zero}}(P_{\text{ref},i}) u_{\text{zero}}(P_{\text{ref},j}) \delta_{k_i k_j} \delta_{l_i l_j} \\ = u_{\text{zero}}(k_i, l_i) u_{\text{zero}}(k_j, l_j) \delta_{k_i k_j} \delta_{l_i l_j}. \quad (\text{B12})$$

Fifth, there is drift uncertainty due to the CDG zero changing with time. To assess the zero drift uncertainty, we log the average zero readings each time that we zero the transfer standard and compute the daily zero drift coefficient B_{kl} for CDG k and gain setting l , averaged across our measurement campaign. For our tightly temperature-controlled transfer standard, the zero drift is approximately monotonic with small discontinuous jumps [10, 34], so we take the covariance matrix for the zero drift as

$$C_{\text{zd}}(P_{\text{ref},i}, P_{\text{ref},j}) = u_{\text{zd}}(P_{\text{ref},i}) u_{\text{zd}}(P_{\text{ref},j}) \delta_{ij} \\ = B_{k_i l_i} (t_i - t_z) B_{k_j l_j} (t_j - t_z) \delta_{ij}, \quad (\text{B13})$$

where t_i is the time of the i th measurement and t_z is the time of the last transfer standard zero. In principle, the zero drift uncertainty is correlated in time with a correlation envelope that decays with $|t_i - t_j|$. However, we are unaware of any systematic studies of the zero drift correlation time of CDGs, so we use the more conservative estimate of Eq. (B13), as suggested by the results of Ref. [10, 34].

Sixth, there is uncertainty in the calibration of the DMM that records the transfer standard readings. We have verified that the DMM meets its 90 day accuracy specification using a calibrated voltage standard. The 90 day accuracy specification for our operating voltage range is 20 $\mu\text{V}/\text{V}$ of reading. After propagating the uncertainty to P_{ref} , the calibration uncertainty corresponds to a fractional pressure uncertainty of approximately 20 $\mu\text{Pa}/\text{Pa}$, which is negligible compared to other sources of uncertainty (see Fig. 7). The DMM also exhibits a 50 μV uncertainty due to the resolution of its analog-to-digital converter, but this uncertainty is random and thus already contained within the covariance matrix of the type A uncertainty above.

Seventh, there is uncertainty in the thermal transpi-

ration correction to P'_{ref} . The transfer standard is stabilized to 23.78(1) $^{\circ}\text{C}$ while the vacuum system has a nominal temperature of 21 $^{\circ}\text{C}$. We therefore correct P'_{ref} for the thermal-transpiration-induced pressure gradient between the transfer standard and the optomechanical sensor using the Takaishi-Sensui equation [35, 52, 53]. The Takaishi-Sensui equation depends on the pressure measured by the transfer standard, the transfer standard temperature, and the vacuum chamber temperature. In principle, uncertainties in each of the above quantities impact the thermal transpiration correction uncertainty. However, the measured pressure uncertainty and vacuum chamber temperature uncertainty have already been included in the analysis above and in Appendix B 1, respectively. Because the uncertainties in these quantities are perfectly self-correlated, we do not include them here to avoid double counting. The uncertainty in the transfer standard temperature is less than 1 mK during a 5 repeat measurement of Γ_t , which corresponds to a fractional thermal transpiration correction uncertainty less than 2 $\mu\text{Pa}/\text{Pa}$. The thermal transpiration correction uncertainty is thus negligible compared to other sources of uncertainty (see Fig. 7).

-
- [1] F. Zhou, Y. Bao, R. Madugani, D. A. Long, J. J. Gorman, and T. W. LeBrun, Broadband thermomechanically limited sensing with an optomechanical accelerometer: Supplement, *Optica* **8**, 350 (2021).
- [2] T. P. Purdy, K. E. Grutter, K. Srinivasan, and J. M. Taylor, Quantum correlations from a room-temperature optomechanical cavity, *Science* **356**, 1265 (2017).
- [3] T. Briant, S. Krenek, A. Cupertino, F. Loubar, R. Braive, L. Weituschat, D. Ramos, M. J. Martin, P. A. Postigo, A. Casas, R. Eisermann, D. Schmid, S. Tabandeh, O. Hahtela, S. Pourjamal, O. Kozlova, S. Kroker, W. Dickmann, L. Zimmermann, G. Winzer, T. Martel, P. G. Steeneken, R. A. Norte, and S. Briaudeau, Photonic and Optomechanical Thermometry, *Optics* **3**, 159 (2022).
- [4] C. Zhao, Q. Yuan, L. Fang, X. Gan, and J. Zhao, High-performance humidity sensor based on a polyvinyl alcohol-coated photonic crystal cavity, *Optics Letters* **41**, 5515 (2016).
- [5] M. Metcalfe, Applications of cavity optomechanics, *Applied Physics Reviews* **1**, 031105 (2014).
- [6] N. Klimov, T. Purdy, and Z. Ahmed, Towards replacing resistance thermometry with photonic thermometry, *Sensors and Actuators A: Physical* **269**, 308 (2018).
- [7] A. J. Fleisher, Z. Ahmed, T. Herman, and M. R. Hartings, Dual electro-optic frequency comb photonic thermometry, *Optics Letters* **48**, 2210 (2023).
- [8] K. Han, D. A. Long, S. M. Bresler, J. Song, Y. Bao, B. J. Reschovsky, K. Srinivasan, J. J. Gorman, V. A. Aksyuk, and T. W. LeBrun, Low-power, agile electro-optic frequency comb spectrometer for integrated sensors, *Optica* **11**, 392 (2024).
- [9] J. K. Fremerey, The spinning rotor gauge, *Journal of Vacuum Science and Technology A* **3**, 1715 (1985).
- [10] R. W. Hyland and C. R. Tilford, Zero stability and calibration results for a group of capacitance diaphragm gages, *Journal of Vacuum Science & Technology A* **3**, 1731 (1985).
- [11] M. Salimi, R. V. Nielsen, H. B. Pedersen, and A. Dantan, Squeeze film absolute pressure sensors with sub-millipascal sensitivity (2024), [arxiv:2312.11915](https://arxiv.org/abs/2312.11915).
- [12] L. Magrini, P. Rosenzweig, C. Bach, A. Deutschmann-Olek, S. G. Hofer, S. Hong, N. Kiesel, A. Kugi, and M. Aspelmeyer, Real-time optimal quantum control of mechanical motion at room temperature, *Nature* **595**, 373 (2021).
- [13] D. S. Barker, D. Carney, T. W. LeBrun, D. C. Moore, and J. M. Taylor, Collision-resolved pressure sensing, *Physical Review A* **109**, 042616 (2024).
- [14] J. Scherschligt, J. A. Fedchak, Z. Ahmed, D. S. Barker, K. Douglass, S. Eckel, E. Hanson, J. Hendricks, N. Klimov, T. Purdy, J. Ricker, R. Singh, and J. Stone, Review Article: Quantum-based vacuum metrology at the National Institute of Standards and Technology, *Journal of Vacuum Science & Technology A* **36**, 040801 (2018).
- [15] C. P. Blakemore, D. Martin, A. Fieguth, A. Kawasaki, N. Priel, A. D. Rider, and G. Gratta, Absolute pressure and gas species identification with an optically levitated rotor, *Journal of Vacuum Science & Technology B* **38**, 024201 (2020).
- [16] C. Reinhardt, H. Masalehdan, S. Croatto, A. Franke, M. B. K. Kunze, J. Schaffran, N. Sülmann, A. Lindner, and R. Schnabel, Self-Calibrating Gas Pressure Sensor with a 10-Decade Measurement Range, *ACS Photonics* **11**, 1438 (2024).
- [17] G. Comsa, J. K. Fremerey, B. Lindenau, G. Messer, and P. Roehl, Calibration of a spinning rotor gas friction

- gauge against a fundamental vacuum pressure standard, *Journal of Vacuum Science & Technology* **17**, 642 (1980).
- [18] K. Jousten, M. Bernien, F. Boineau, N. Bundaleski, C. Illgen, B. Jenninger, G. Jönsson, J. Šetina, O. M. Teodoro, and M. Vičar, Electrons on a straight path: A novel ionisation vacuum gauge suitable as reference standard, *Vacuum* **189**, 110239 (2021).
- [19] Y. Tsaturyan, A. Barg, E. S. Polzik, and A. Schliesser, Ultracoherent nanomechanical resonators via soft clamping and dissipation dilution, *Nature Nanotechnology* **12**, 776 (2017).
- [20] R. G. Christian, The theory of oscillating-vane vacuum gauges, *Vacuum* **16**, 175 (1966).
- [21] A. Cavalleri, G. Ciani, R. Dolesi, M. Hueller, D. Nicolodi, D. Tombolato, S. Vitale, P. J. Wass, and W. J. Weber, Gas damping force noise on a macroscopic test body in an infinite gas reservoir, *Physics Letters A* **374**, 3365 (2010).
- [22] L. Martinetz, K. Hornberger, and B. A. Stickler, Gas-induced friction and diffusion of rigid rotors, *Physical Review E* **97**, 052112 (2018).
- [23] H. Hosaka, K. Itao, and S. Kuroda, Damping characteristics of beam-shaped micro-oscillators, *Sensors and Actuators A* **49**, 87 (1995).
- [24] J. Lübke, M. Temmen, H. Schnieder, and M. Reichling, Measurement and modelling of non-contact atomic force microscope cantilever properties from ultra-high vacuum to normal pressure conditions, *Measurement Science and Technology* **22**, 055501 (2011).
- [25] Eventually, the size of the chamber enclosing the oscillator will also affect the damping rate, see Ref. [9, 54].
- [26] W. E. Newell, Miniaturization of Tuning Forks, *Science* **161**, 1320 (1968).
- [27] BIPM, IEC, IFCC, ILAC, ISO, IUPAC, IUPAP, and OIML, *International vocabulary of metrology — Basic and general concepts and associated terms (VIM)*, Joint Committee for Guides in Metrology, JCGM 200:2012. (3rd edition) ().
- [28] N. F. Ramsay, *Molecular Beams* (Oxford University Press Inc., New York, 1956).
- [29] P. F. Egan, J. A. Stone, J. H. Hendricks, J. E. Ricker, G. E. Scace, and G. F. Strouse, Performance of a dual Fabry – Perot cavity refractometer, *Optics Letters* **40**, 3945 (2015).
- [30] P. F. Egan, J. A. Stone, J. E. Ricker, and J. H. Hendricks, Comparison measurements of low-pressure between a laser refractometer and ultrasonic manometer, *Review of Scientific Instruments* **87**, 053113 (2016).
- [31] D. S. Barker, J. A. Fedchak, J. Klos, J. Scherschligt, A. A. Sheikh, E. Tiesinga, and S. P. Eckel, Accurate measurement of the loss rate of cold atoms due to background gas collisions for the quantum-based cold atom vacuum standard, *AVS Quantum Science* **5**, 035001 (2023).
- [32] F. Nakao, Determination of the ionization gauge sensitivity using the relative ionization cross-section, *Vacuum* **25**, 431 (1975).
- [33] K. Jousten, S. Bechstein, M. Bernien, F. Boineau, N. Bundaleski, C. Illgen, B. Jenninger, J. Šetina, R. A. Silva, A. Stöltzel, O. M.N.D. Teodoro, and M. Wüest, Evaluation and metrological performance of a novel ionisation vacuum gauge suitable as reference standard, *Measurement* **210**, 112552 (2023).
- [34] A. P. Miller, Measurement performance of capacitance diaphragm gages and alternative low-pressure transducers, *NCSL Workshop & Symposium* , 287 (1997).
- [35] J. Ricker, J. Hendricks, T. Bock, k. Dominik, T. Kobata, J. Torres, and I. Sadkovskaya, Final report on the key comparison CCM.P-K4.2012 in absolute pressure from 1 Pa to 10 kPa, *Metrologia* **54**, 07002 (2017).
- [36] C. Reinhardt, T. Müller, A. Bourassa, and J. C. Sankey, Ultralow-Noise SiN Trampoline Resonators for Sensing and Optomechanics, *Physical Review X* **6**, 021001 (2016).
- [37] R. A. Norte, J. P. Moura, and S. Gröblacher, Mechanical Resonators for Quantum Optomechanics Experiments at Room Temperature, *Physical Review Letters* **116**, 147202 (2016).
- [38] Certain commercial equipment, instruments, or materials are identified for reference purposes only. Such identification is not intended to imply recommendation or endorsement by NIST, nor is it intended to imply that the materials or equipment identified are necessarily the best available for the purpose.
- [39] BIPM, IEC, IFCC, ILAC, ISO, IUPAC, IUPAP, and OIML, *Evaluation of measurement data — Guide to the expression of uncertainty in measurement*, Joint Committee for Guides in Metrology, JCGM 100:2008 ().
- [40] A. Markwitz, H. Baumann, E. F. Krimmel, K. Bethge, and P. Misaelides, Characterisation of thin sputtered silicon nitride films by NRA, ERDA, RBS and SEM, *Fresenius' Journal of Analytical Chemistry* **346**, 177 (1993).
- [41] R. Huszank, L. Csedreki, Z. Kertész, and Z. Török, Determination of the density of silicon–nitride thin films by ion-beam analytical techniques (RBS, PIXE, STIM), *Journal of Radioanalytical and Nuclear Chemistry* **307**, 341 (2016).
- [42] X-ray Microscopy Windows Specification Sheet, <https://www.norcada.com/wp-content/uploads/2013/10/Xray-Window-Specsheet.pdf>.
- [43] M. A. Pickering, R. L. Taylor, J. T. Keeley, and G. A. Graves, Chemically vapor deposited silicon carbide (SiC) for optical applications, *Nuclear Instruments and Methods in Physics Research A* **291**, 95 (1990).
- [44] J. S. Goela, M. A. Pickering, R. L. Taylor, B. W. Murray, and A. Lompadó, Properties of chemical-vapor-deposited silicon carbide for optics applications in severe environments, *Applied Optics* **30**, 3166 (1991).
- [45] W. M. Trott, J. N. Castañeda, J. R. Torczynski, M. A. Gallis, and D. J. Rader, An experimental assembly for precise measurement of thermal accommodation coefficients, *Review of Scientific Instruments* **82**, 035120 (2011).
- [46] F. Sharipov and M. R. Moldover, Energy accommodation coefficient extracted from acoustic resonator experiments, *Journal of Vacuum Science & Technology A* **34**, 061604 (2016).
- [47] M. Schmelling, Averaging correlated data, *Physica Scripta* **51**, 676 (1995).
- [48] P. Bevington and D. Robinson, *Data Reduction and Error Analysis for the Physical Sciences*, Book and Disk No. v. 1 (McGraw-Hill, 1992).
- [49] D. Foreman-Mackey, D. W. Hogg, D. Lang, and J. Goodman, Emcee: The MCMC Hammer, *Publications of the Astronomical Society of the Pacific* **125**, 306 (2013).
- [50] E. Romero, V. M. Valenzuela, A. R. Kermany, L. Sementilli, F. Iacopi, and W. P. Bowen, Engineering the Dissipation of Crystalline Micromechanical Resonators, *Physical Review Applied* **13**, 044007 (2020).
- [51] D. Shin, A. Cupertino, M. H. de Jong, P. G. Steeneken, M. A. Bessa, and R. A. Norte, Spiderweb Nanomechan-

- ical Resonators via Bayesian Optimization: Inspired by Nature and Guided by Machine Learning, *Advanced Materials* **34**, 2106248 (2022).
- [52] K. F. Poulter, M.-J. Rodgers, P. J. Nash, T. J. Thompson, and M. P. Perkin, Thermal transpiration correction in capacitance manometers, *Vacuum* **33**, 311 (1983).
- [53] T. Takaishi and Y. Sensui, Thermal transpiration effect of hydrogen, rare gases and methane, *Transactions of the Faraday Society* **59**, 2503 (1963).
- [54] G. Reich, Spinning rotor viscosity gauge: A transfer standard for the laboratory or an accurate gauge for vacuum process control, *Journal of Vacuum Science and Technology* **20**, 1148 (1982).